ORIGINAL RESEARCH ARTICLE

Understanding the Structure and Electrochemical Behavior of the Rust Layer Formed on a High-Strength Low-Alloy Structural Steel under Cyclic Exposure to Polluted Marine Atmosphere

Amulya Bihari Pattnaik, Subhnit Roy, V. Srinivasa Raja, and Smrutiranjan Parida

The surface rust layer of ASTM A572 grade 50 high-strength low-alloy structural steel was examined under laboratory wet/dry cyclic corrosion test (CCT) conditions in a simulated polluted marine environment. According to the corrosion kinetics study, the entire corrosion process in the sample occurred in four stages, which were identified by the power law exponent, evolved phases, and electrochemical behavior of the rust layer at various stages. During the early stages of corrosion, the reduction of rust layer phases and the anodic dissolution of the steel substrate accelerated the overall corrosion rate. Variations in the corrosion rate were observed as the composition of the rust layer stabilized with increasing CCT cycle due to cracking and self-repairing of the rust layer. At higher CCT, the composition of the rust layer gradually changed from a conductive γ-FeOOH phase to a stable α-FeOOH phase. The electrochemical impedance analysis also revealed an increase in rust layer resistance as well as charge transfer resistance of side reactions such as hydrogen evolution reaction (HER). As a result, as CCT increased, corrosion resistance and thus the protective ability index increased (PAI). The defect density in the semiconducting rust layer formed at higher CCT was lower, indicating a higher level of protection. Based on the findings, a plausible mechanism of growth of the protective rust layer on the steel sample was proposed.

1. Introduction

Due to their superior mechanical properties, high-strength low-alloy structural steels are widely used in structural applications such as cranes, building structures, heavy construction equipment, and bridges (Ref 1, 2). Corrosion degradation occurs as a result of the harsh industrial and marine environments to which these steels are frequently exposed (Ref 3, 4). In light of rapid industrial expansion over the past two decades and increased emphasis on environment and sustainability, understanding the atmospheric corrosion behavior of these steels to improve their performance is crucial (Ref 5).

Amulya Bihari Pattnaik, Subhnit Roy, V. Srinivasa Raja, and **Smrutiranjan Parida**, Department of Metallurgical Engineering and Materials Science, Indian Institute of Technology Bombay, Powai, Mumbai, Maharashtra 400076, India. Contact e-mail: paridasm@iitb.ac.in.

Many researchers have extensively studied the atmospheric corrosion behavior of low carbon and weathering steels under both field and laboratory conditions (Ref 6-9). Different rust formation mechanisms have been proposed for these steels, depending on the environments to which they are exposed. However, there is a general agreement regarding the constituents of the rust layer and their protective nature. Extensive research work in atmospheric corrosion of steel has led to identifying α-FeOOH (Goethite), γ-FeOOH (Lepidocrocite), β-FeOOH (Akageneite), and Fe_3O_4 (Magnetite) as the major constituents of the rust layers. Yamashita et al. (Ref 10), in their study on the atmospheric corrosion behavior of mild steel and weathering steel in an industrial atmosphere, found that the rust layer formed consisted of an outer layer of γ-FeOOH and an inner layer of densely packed fine α-FeOOH. They also proposed a factor called the protective ability index (PAI) to relate the phase formed in the rust layer to the atmospheric corrosion resistance of the steel. Accordingly, PAI was determined based on the ratio of the mass fraction of the goethite/lepidocrocite (i.e., α/γ), which can be related to the resistance of steels to atmospheric corrosion. A higher PAI means higher atmospheric corrosion resistance of steel which depends on the exposure time and the corrosivity environment. Oh et al. (Ref 11), in their study, identified the α-FeOOH and γ-FeOOH as the major constituents of the rust layers formed in different low-carbon steels. In low alloy and plain carbon steels, the nature of the rust layer has been found to be strongly dependent upon the nature of the environment to which the steels are exposed (Ref 12). Indoor studies conducted on plain carbon steel for forty years indicate that α-FeOOH is the most

stable phase formed in the rust layer (Ref 13). The role of rust layer thickness on the atmospheric corrosion behavior of a 690 MPa construction steel in a simulated industrial atmosphere was studied by Wenting Zhu et al. (Ref 14). The electrochemical behavior of the rust formed on the steel suggests that the diffusion of corrosive ions decreases with the increase in rust layer thickness. Liu et al. (Ref 15) studied the effect of tin on the corrosion behavior of low-alloy steel in a simulated coastal-industrial atmosphere for 120 CCT. They found that the addition of tin increases the corrosion resistance of the steel substrate due to the formation of a more stable α-FeOOH phase in the rust layer. They also observed that the corrosion of the steel followed three different corrosion kinetics with the CCT. Initially, there was a rapid increase in the kinetics, and then, in the second and third stages, the kinetics decreased at varying rates. The corrosion rate in the second and third stages decreases owing to the formation of a stable α-FeOOH phase in the rust layer. They have also shown that the corrosion process in an acidic environment is accompanied by two cathodic reactions, the oxygen reduction reaction (ORR) and the hydrogen evolution reaction (HER). Evans et al. (Ref 16) proposed that during atmospheric rusting, both γ-FeOOH and β-FeOOH phases of the rust layer can be reduced during the wetting stage of the steel, supported by the anodic oxidation, $Fe \rightarrow Fe^{2+} + 2e^-$. The oxygen reduction and/or hydrogen evolution reactions are typical cathodic processes in an acidic environment. These processes are now accompanied by the cathodic reduction of the rust layer. Under this situation, the corrosion rate of the steel will be controlled by all three processes. This means that further research is needed to fully comprehend the electrochemical nature of rust layer formation and its relationship to the corrosion rate of steel under atmospheric exposure.

Atmospheric corrosion of steel is too critical in industrial and coastal areas. The presence of a high concentration of airborne pollutants like sulfur dioxide (SO_2) and aggressive ions like chloride ions (Cl^-) affects the nature of the rust layer (Ref 12). The ingress of aggressive Cl^- ions into the rust layer causes loose, porous, and less adherent rust, bringing the steel surface in contact with the electrolyte solution, thus increasing the corrosion rate (Ref 17, 18). It has been observed that the presence of Cl^- ions could break the rust layer (Ref 19), whereas SO_2 promotes the formation of stable α-FeOOH during the initial stages of the corrosion process (Ref 20). However, an increase in the SO_2 concentration, with time, has a detrimental effect on the rust layer protection properties. From the above studies, the presence of aggressive ions like Cl^- and SO_4^{2-} has been shown to synergistically affect the nature of the rust layer and its protective ability in the case of low-alloy steels. To fully evaluate its corrosion behavior in a polluted marine atmosphere and predict its useful life, the effect of these ions on the rust formed on the high-strength low-alloy steel is required.

To characterize the rust layer formed on steels, various surface characterization techniques have been used (Ref 8, 9). To determine elemental composition, scanning electron microscopy (SEM)–energy-dispersive x-ray (EDX) analysis is used. X-ray diffraction (XRD) and infrared spectroscopy (IR) are used to identify the phases of corrosion products. Many researchers have recently used micro-Raman spectroscopy to determine corrosion product phases because it can detect amorphous phases (Ref 21-23). The combination of micro-Raman spectroscopy and an optical microscope provides an efficient method for determining the structure and depth profiling of the rust layer.

Outdoor/field exposure tests are considered the most accurate to study the atmospheric corrosion process. However, these tests are time-consuming in nature. Therefore, the laboratory-based wet/dry cyclic corrosion test (CCT) that produces adherent rust layer similar to those formed in outdoor tests in short time intervals is one of the most useful approaches to understand the atmospheric corrosion of steel (Ref 24-29). Therefore, the corrosion behavior of a high-strength low-alloy structural steel (ASTM A572 grade 50) micro-alloyed with niobium (Nb) and vanadium (V) was studied using a laboratory-based wet/dry cyclic corrosion test to gain a better understanding of the electrochemical nature of the rust layer formed in a polluted marine environment and its relationship to the rust layer's composition. As per the author's knowledge, no comprehensive study has been carried out on this material to study the corrosion behavior in a simulated polluted marine atmosphere. The structure of the rust layer was studied using grazing incidence x-ray diffraction (GI-XRD), field emission scanning electron microscopy (FESEM), and micro-Raman spectroscopy. The electrochemical nature of the rust layer was studied using electrochemical impedance spectroscopy (EIS), and the defect structure of the rust layer was studied using the Mott-Schottky (MS) analysis.

2. Experimental

2.1 Materials

ASTM A572 grade 50 high-strength low-alloy structural steel supplied by Steel Authority of India Limited (SAIL), Rourkela, Odisha, India having tensile and yield strengths of 450 and 345 MPa respectively was studied. The steel is micro-alloyed with Nb, V to ensure grain refinement and precipitation hardening. The composition of the steel was determined using optical emission spectroscopy (SPECTROMAXx LMX07, SPECTRO Analytical Instruments Inc. USA) is given in Table 1. A typical optical micrograph revealing the microstructure of the steel is shown in Figure 1.

The alloy has a banded microstructure with alternate layers of ferrite and pearlite. Specimens of $10 \times 10 \times 1$ mm were used for gravimetric and electrochemical studies and to characterize the formed rust layer. For gravimetric studies, the specimens were ground with SiC emery papers down to 1200 grit silicon carbide paper. Further, the samples were cleaned ultrasonically using ethanol and stored in a moisture-free desiccator before they were used for further studies. In gravimetric studies, four specimens were used to check for reproducibility of the data.

2.2 Wet/dry Cyclic Corrosion Test

Due to its resemblance to actual outdoor corrosion, the wet/dry cyclic corrosion test is regarded as an appropriate method for simulating atmospheric corrosion (Ref 14, 15). The exposed samples after the cyclic corrosion test were used for the study of rust layer characterization and to evaluate the corrosion kinetics. The environment opted for the study was the simulated polluted marine atmosphere with the following constitution, 3.5 wt.% NaCl + 0.01 M NaHSO$_3$ with pH = 3.8 $\pm$ 0.1 at 30 °C (Ref 14). For the cyclic corrosion study, the

Table 1 Chemical composition of ASTM A572 grade 50 steel

Elements	C	Mn	Ni	S	P	Si	Nb	V	Fe
wt.%	0.15	1.32	0.072	0.02	0.02	0.32	0.02	0.02	Bal.
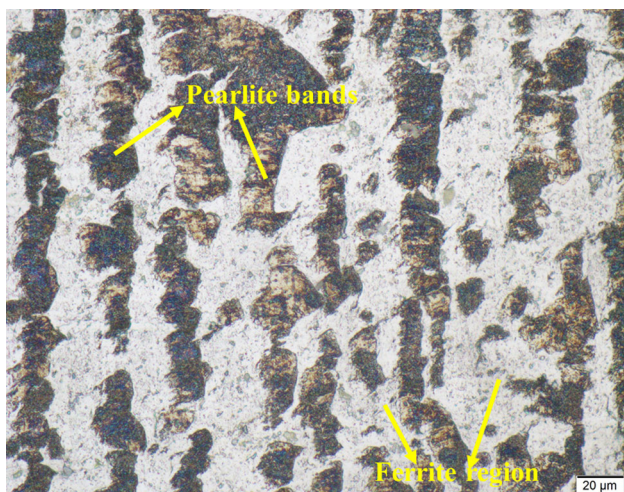
Fig. 1 Optical micrograph of ASTM A572 grade 50 steel

relative humidity inside the chamber was retained at 75% ($\pm$ 5%). Cyclic corrosion test was conducted by the following steps (Ref 30-32): (i) Initially weighing the bare samples; (ii) the surface of the sample was dampened with a dosage of 40 μl/cm^2 3.5 wt.% NaCl + 0.01 M NaHSO$_3$ that simulated a polluted marine atmosphere; (iii) samples were placed inside a humidity chamber; (iv) after a period of 12 h samples were weighed; (v) the surface of the samples was rinsed with deionized water to avert the salt amassing. Also, it should be noted that rinsing should be done carefully to prevent rust loss. The procedure mentioned above was repeated for a total of 120 cycles. The schematic of the wet/dry cyclic corrosion test procedure is shown in Fig. 2.

2.3 Rust layer Characterization

An Olympus GX 53 inverted optical microscope (Olympus Corporation, Japan) was used to analyze the microstructure of the steel specimens. A PanAlytical^{TM} MRD x-ray diffraction (Malvern Panalytical, UK) unit was used to perform GI-XRD to identify the phases of the rust layer. The GI-XRD was carried out with an incidence angle of ω = 2° and a 2θ range of 20°-90°. Cross-sectional image of the rust layer was studied using a JSM-7600F FESEM (JEOL, Japan) equipped with an EDX. The nature of the phases formed in the rust layers were also analyzed using a LabRAM HR Evolution (HORIBA, France) Raman spectrometer. The samples were excited using a 532 nm He-Ne laser. The laser power was kept below 1 mW to avoid heating of the specimen.

2.4 Electrochemical Measurements

Steel specimens of dimension 10 $\times$ 10 $\times$ 1 mm were used for electrochemical tests. Working electrodes were prepared by shouldering copper wire on the counter surface of the steel specimen covered with a rust layer and covering all the surfaces

except the one with rust layer with a polymer resin. The exposed surface area of the electrode was 1 $\times$ 1 cm^2. A solution of 3.5 wt.% NaCl + 0.01 M NaHSO$_3$ was prepared using analytical grade reagents and deionized water for corrosion studies. The electrochemical measurements were carried out using a VERSASTAT 4.0 potentiostat (Princeton Applied Research, USA) and the data were analyzed using the VERSASTUDIO software. Saturate calomel electrode (SCE) as a reference electrode, and platinum as the counter electrode along with the steel working electrode were used in the corrosion cell. The working electrode's open circuit potential (OCP) was measured till stabilization occurred which took about 30 minutes. The EIS was carried out at OCP with an AC signal amplitude of 10 mV and a frequency range of 10^5-10^{-2} Hz. The defect concentration of the rust layer was studied using the Mott–Schottky (MS) analysis. The measurements for MS analysis were carried out at a frequency of 1 kHz within a potential range of $-$ 0.5 to $-$ 1.5 V_{SCE} with a step size of 50 mV in the cathodic region. The frequency of 1 kHz for Mott-Schottky was used for a similar type of materials in literature (Ref 33-41). All tests have been performed at least in triplicate to check for data reproducibility.

3. Results and Discussion

3.1 Corrosion Kinetics and Stages of Corrosion

Figure 3 depicts the progression of weight gain and the instantaneous corrosion rate with CCT cycles for high-strength low-alloy structural steel ASTM A572 grade 50 exposed to a simulated polluted marine atmosphere.

The weight gain increased monotonously up to 70 CCT with some fluctuation in the middle followed by a slow change. Correspondingly, a nonlinear atmospheric corrosion behavior was observed with a rapid increase in corrosion rate up to 3 CCT, followed by a sharp decrease up to 17 CCT, after which it varied with fluctuations and then further declined after 80 CCT as depicted in Fig. 3.

The atmospheric corrosion kinetics were fitted using the power law shown below (Ref 42-44).

$$\Delta W = AN^n \qquad \text{(Eq 1)}$$

where ΔW represents weight gain (mg/cm^2), N represents the number of CCT cycles and A and n are constants. The above equation suggests that the corrosion behavior strongly depends upon two factors: A which depicts the initial corrosion rate of the steel, and n is the power law exponent, which indicates the physicochemical behavior of the rust layer (Ref 44, 45). The power function was expressed as a bi-logarithmic equation, and Fig. 4 represents a log-log plot of weight gain versus CCT, demonstrating that atmospheric corrosion occurred in stages. Table 2 shows the parameters A and n at various stages of corrosion that were obtained by fitting the curve to the power law.
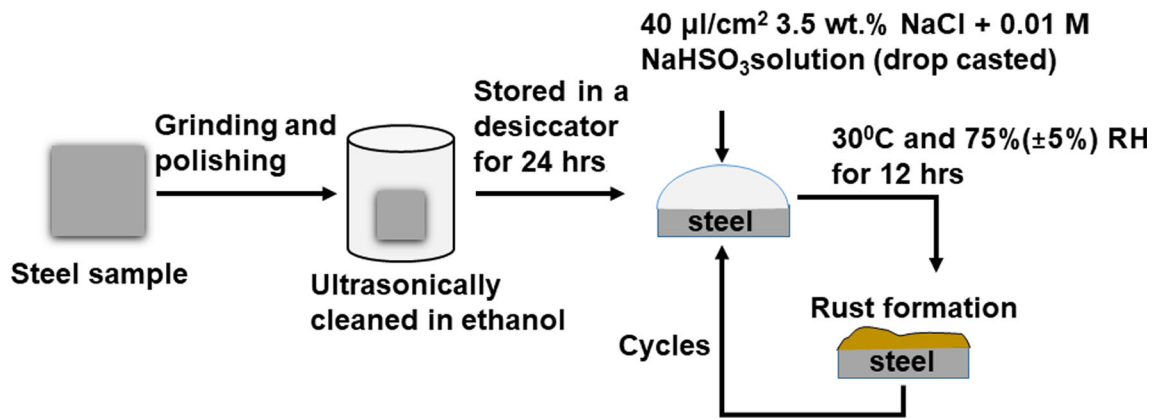
Fig. 2 Schematic of the steps involved in conducting wet/dry cyclic test
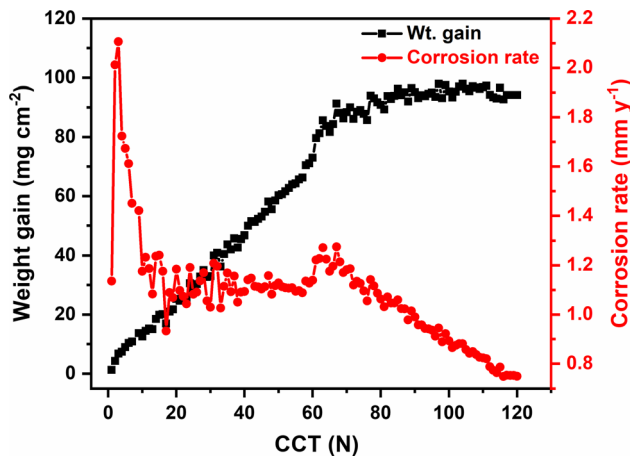

Fig. 3 Variation of weight gain and corrosion rate vs. CCT of steel sample exposed to simulated polluted marine atmosphere

From the values of the power law exponent n shown in Table 2, four distinct stages in the corrosion of the steel can be observed. During 1-3 CCT, stage 1, the n value was 1.40, indicating rapid corrosion. The n value in the second stage, 3-17 CCT, was 0.63, significantly lower than that in stage 1, indicating a decrease in corrosion rate during this stage. The n value increased to 0.97 in the third stage, 17-80 CCT, indicating a stable region owing to the formation of a thicker rust layer. However, at the fourth stage, 80-120 CCT, the n value dropped significantly to 0.14, indicating a significant decrease in the corrosion rate, as depicted in Fig. 3. The nature of the rust layer formed was investigated and related to the corrosion behavior in different stages.

3.2 Rust Layer Characteristics

The oxide phases in the corrosion products on the surface of the steel were studied using GI-XRD analysis which is shown in Fig. 5(a). Different iron oxides and oxyhydroxide phases such as α-FeOOH, γ-FeOOH, α-Fe$_2$O$_3$, and Fe$_3$O$_4$ were detected.

Figure 5(a) shows that the initial corrosion product formed on the steel surface after 5 CCT mainly consisted of γ-FeOOH and Fe$_3$O$_4$. However, as the CCT progressed up to 120 CCT, the number of α-FeOOH peaks increased, indicating a stable rust layer formation. The latter observation was also

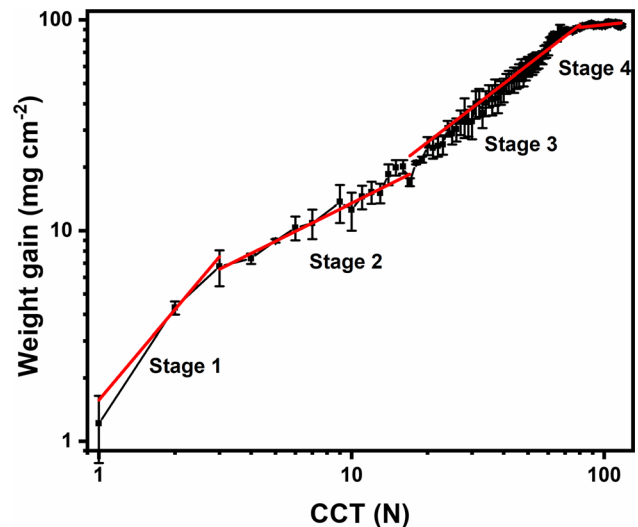**Fig. 4** Log ΔW vs. log CCT plot obtained the steel exposed to the simulated polluted marine atmosphere

reported in several other studies (Ref 10-12). The protective ability index (PAI) of steel has been related to the α/γ ratio (Ref 8, 10, 11, 30). The ratio was calculated from the phase fractions of α and γ obtained using the X'Pert Highscore Plus software in which the Relative Intensity Ratio (RIR) of the phases in relation to the internal standard substance (Al$_2$O$_3$) was used (Ref 46, 47). Figure 5(b) shows the phase fractions and PAI in terms of α/γ ratio. The fraction of α-FeOOH and γ-FeOOH, which was high at the beginning, decreased after 15 CCT and increased further with the increase in the CCT number (Fig. 5b). The decrease in the fraction of α-FeOOH and γ-FeOOH at 15 CCT can be attributed to the formation of phases like Fe$_3$O$_4$. The α-FeOOH phase fraction increased and reached a maximum at 40 CCT, and thereafter, it did not change up to 80 CCT. A slight decrease at 120 CCT was probably due to the cracking and reformation of the rust layer. The GI-XRD results indicated that at higher CCT, γ-FeOOH phase fraction decreased and that of α-FeOOH increased due to the former getting converted to more stable α-FeOOH (Ref 10-12, 25). Hence, at higher CCT, the rust layer becomes more stable and compact due to the predominance of α-FeOOH. Correspondingly, the figure also suggests an increase in the protectiveness of the rust layer (hence the decrease in the corrosion rate) with

Table 2 Log-log fitting data of weight gain versus Number of CCT cycles of the steel

	Stage 1	Stage 2	Stage 3	Stage 4
Number of CCT cycles	1 to 3	3 to 17	17 to 80	80 to 120
Equation: $\log\Delta W = \log A + n\log N$	$\log\Delta W = 0.34 + 1.4\log N$	$\log\Delta W = 0.56 + 0.63\log N$	$\log\Delta W = 0.28 + 0.97\log N$	$\log\Delta W = 1.73 + 0.14\log N$
Slope (n)	1.40	0.63	0.97	0.14
R^2	0.94	0.97	0.98	0.99
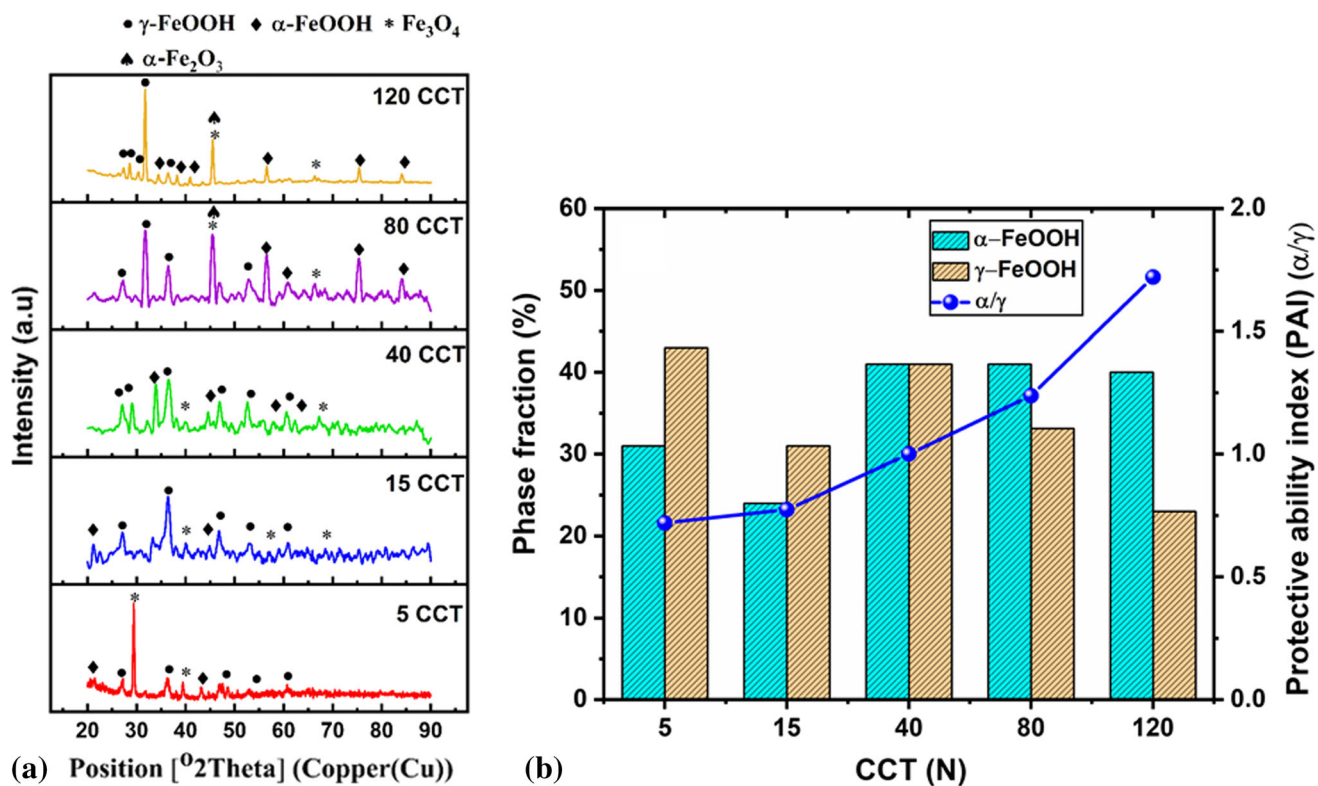
Fig. 5 GI-XRD results depicting the (a) phase composition and (b) semi-quantitative analysis of the phase fraction in the rust layer and protective ability index

the increase in the CCT cycles. The PAI for 120 CCT was 1.72 whereas, for 5 CCT, it was 0.72.

Using line scan in micro-Raman spectroscopy the composition of the rust layer and their layer structure across the thickness was explored. The line scan was conducted across the thickness of the rust layer on the steel specimens exposed to 15 and 120 CCT as delineated in Fig. 6.

The thickness of the rust layer formed on the steel specimen below 15 CCT was insufficient to accurately identify the phases using the micro-Raman technique. The characteristic Raman shifts (cm^{-1}) for different phases in the rust layer are shown in Table 3, which were corroborated from the literature (Ref 48-53). Figure 6(a) shows the Raman line scan spectra of the cross section of rust layer after 15 CCT. Position 1 of the Raman line spectra is located at the outer rust layer, and position 7 is located at the inner rust layer (at the rust–substrate interface). The Raman spectra obtained at position 1 and position 2 showed the presence of Fe_3O_4 and γ-FeOOH. At position 3, Fe_3O_4, γ-FeOOH, and ferrihydrite ($Fe_5HO_8.H_2O$) were found. The Ferrihydrite phase typically occurs with a broad band between 700 and 710, as shown in Table 3.

Raman spectra at positions 4, 5, and 6 showed the presence of Fe_3O_4 and γ-FeOOH. Position 7, which was located at the innermost rust layer, showed the presence of α-FeOOH, γ-FeOOH, γ-Fe$_2$O$_3$, and α-Fe$_2$O$_3$. The Raman point scan along the thickness indicated, the transition of γ-FeOOH phase at the outer surface to the α-FeOOH phase in the inner rust layer of the sample exposed to 15 CCT. However, the rust layer was mostly dominated by γ-FeOOH phase, which is metastable and less protective, which is responsible for the very low PAI value seen in Fig. 5(b). Figure 6(b) shows the Raman spectra obtained from the rust layer formed after 120 CCT. Position 1, located at the outermost rust layer, consisted of Fe_3O_4 and γ-FeOOH. Position 2 showed the existence of ferrihydrite ($Fe_5HO_8.H_2O$) with a broad band at ~ 700 cm^{-1}. The Raman spectra at position 3 were representative of Fe_3O_4 and ferrihydrite. At positions 4, 5, and 6, α-FeOOH and γ-FeOOH were detected with peaks at ~ 385, 285, and ~ 217, respectively. The innermost rust layer at position 7 consists of α-FeOOH, γ-FeOOH, and α-Fe$_2$O$_3$. The rust layer at the 120 CCT sample, thus, showed the presence of α-FeOOH at most layers (positions 4, 5, 6, 7) spanning from the rust–substrate interface
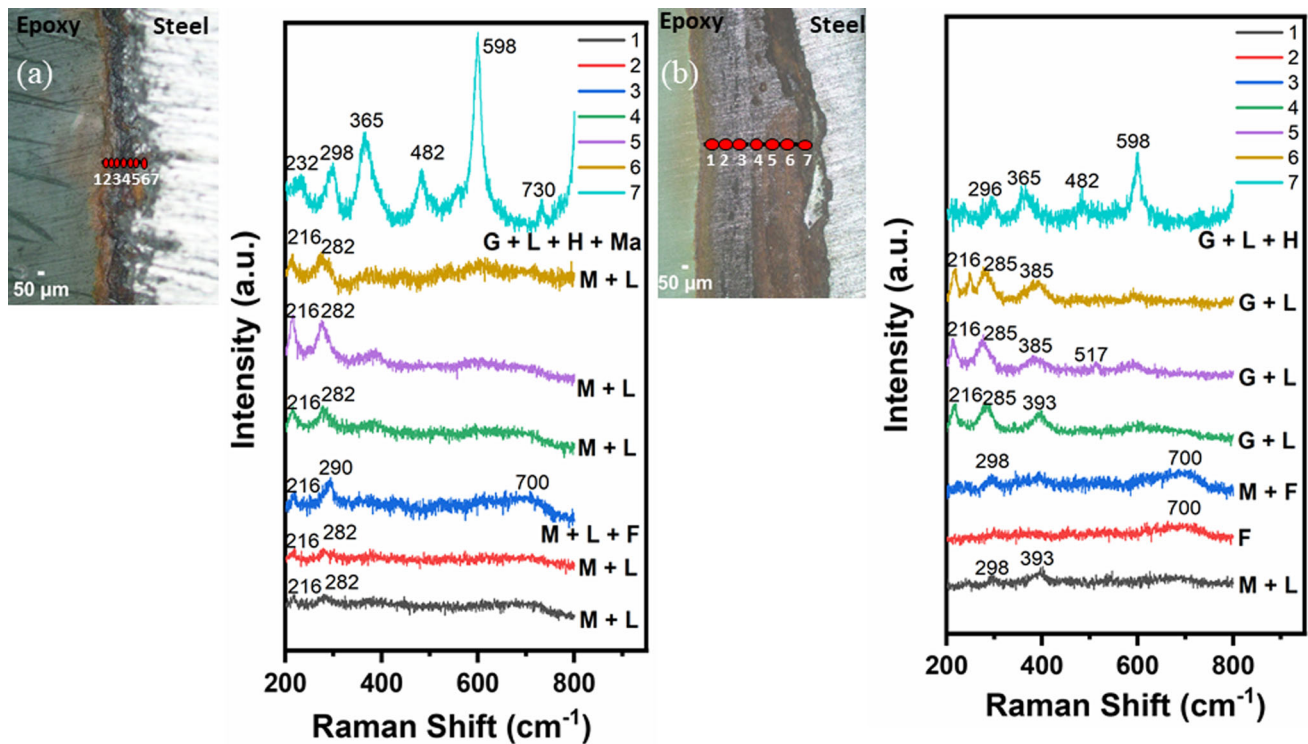
Fig. 6 The cross-sectional Raman line scan spectra through the thickness of the rust layer formed after (a) 15 CCT and (b) 120 CCT (M: Fe_3O_4; L: γ-FeOOH; F: Ferrihydrite $Fe_5HO_8.H_2O$; G: α-FeOOH; Ma: γ-Fe$_2$O$_3$; H: α-Fe$_2$O$_3$)

Table 3 Characteristic Raman shifts (cm^{-1}) for different phases as per literature (Ref 48-53)

Rust layer phases	Raman shifts, cm^{-1}
Lepidocrocite (γ-FeOOH)	217^s, $(248–252)^s$, $(378–380)$, $(528–530)$, $(650–655)$, 713
Goethite (α-FeOOH)	$(241–250)$, $(298–301)$, $(385–390)^s$, $(478–483)$ $(549–552)$, $(680–685)$
Akageneite (β-FeOOH)	$(310–314)^s$, $(385–390)^s$, $(497–499)$, $(538–541)$, $(720–723)$
Feroxyhyte (δ-FeOOH)	$(385–392)$, 400, $(655–680)^s$
Magnetite (Fe_3O_4)	$(298–302)$, $(540–550)$, $(636–670)^s$
Maghemite (γ-Fe$_2$O$_3$)	350, $(500–506)^s$, $(700–720)^s$
Hematite (α-Fe$_2$O$_3$)	$(220–228)^s$, $(240–247)$, $(289–299)^s$, $(400–415)^s$, $(497–502)$, $(609–615)$
Ferrihydrite ($Fe_5HO_8.H_2O$)	Broad band between 700 and 710

^{s}: The strongest peak; Underlined: The next strongest peak.

to the middle of the rust layer. The presence of α-FeOOH across the thickness indicated the formation of a stable and compact rust layer. This explains the high PAI obtained for 120 CCT (Fig. 5b).

The cross-sectional morphologies of the rust layer were further probed by the corresponding elemental distributions in the rust layers formed at 15 CCT and 120 CCT, as shown in Fig. 7.

The thickness of the overall rust layer was about 1181 μm for 120 CCT, thicker than 108 μm seen for 15 CCT. The elemental mapping by EDS also gave an idea about the Cl^- ion impregnation in the rust layer. For the 15 CCT sample, the Cl^- was found close to the steel rust interface, supporting a higher corrosion rate by its action. However, at 120 CCT, the Cl^- was mainly concentrated in the outer to the middle of the rust layer, indicating no penetration to the inner rust layer. Which demonstrated the imperviousness of the inner rust layer in the

case of 120 CCT to the ingress Cl^-. The latter was another evidence of the protectiveness of the rust layer formed at 120 CCT and explained the high PAI.

3.3 Electrochemical Characterization of the Rust Layer

3.3.1 Open Circuit Potential (OCP). Open circuit potential (OCP) has been used to assess the protective nature of rust layers (Ref 54, 55). The OCP of the rusted steel specimens, formed under exposure to different CCT cycles, was measured in 3.5 wt.% NaCl + 0.01 M NaHSO$_3$ (pH $\sim$ 3.8) solution, simulating the polluted marine atmosphere. The OCP was compared with that of the bare steel as presented in Fig. 8(a).

From the figure, at the end of the 1800 s, the OCP steeply raised from $- 0.709$ V_{SCE} for the bare steel to $- 0.54$ V for 40 CCT and remained almost the same till 80 CCT, then slightly raised to $- 0.53$ V_{SCE} for 120 CCT. That means the developed
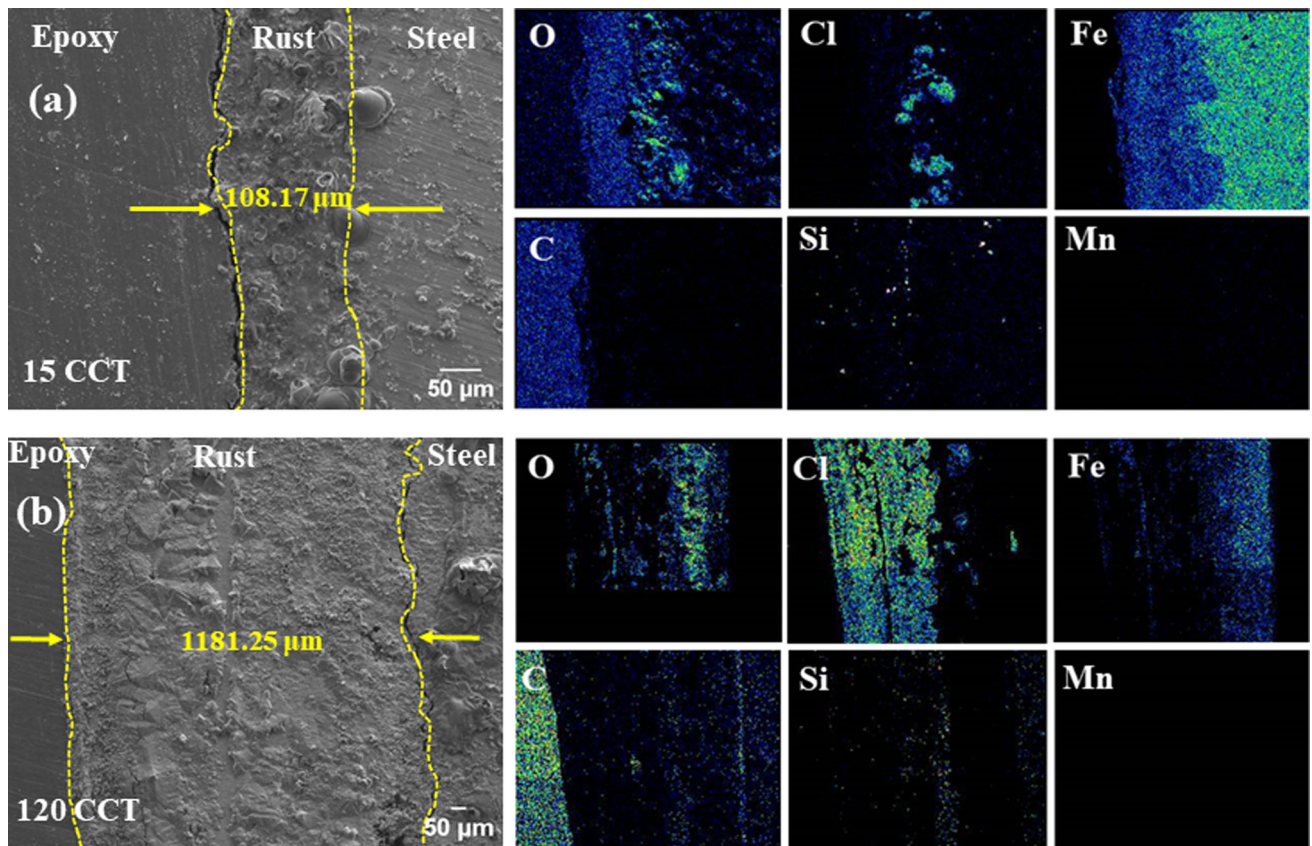
Fig. 7 Cross-sectional morphology and elemental distribution in rust layer exposed to (a) 15 CCT and (b) 120 CCT
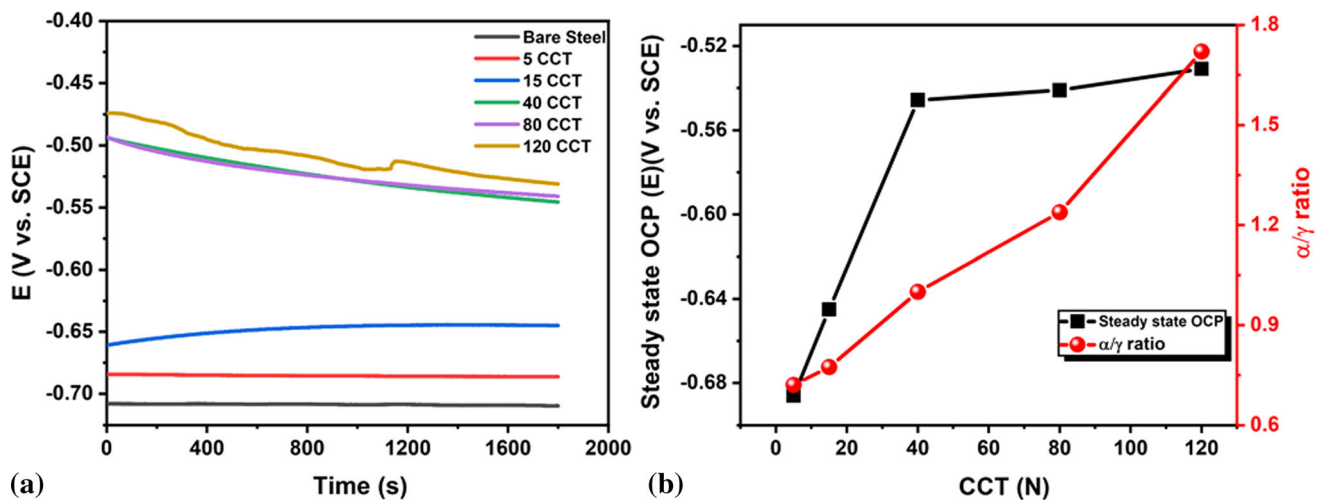

Fig. 8 OCP of the (a) variously rusted and un-rusted steel specimens (b) steady-state OCP and α/γ ratio vs. CCT number

rust layer in the samples exposed to higher CCT cycles displayed noble behavior. The nobler OCP of the rust must be related to the oxide phases formed in the rust layer. As was previously discussed, as the number of CCT cycles increased, the phase fraction of the most protective oxide phase, α-FeOOH, increased, and the fraction of the more conductive phase, γ-FeOOH, decreased. The decrease in the conductive γ-FeOOH phase can be attributed to the increase in OCP with the CCT cycle. This also corroborates an increase in the α/γ ratio

(Fig. 8b). This observation was further supported by the EIS studies discussed in the following section.

3.3.2 Electrochemical Impedance Spectroscopy (EIS). The impedance of the rust layer formed on the steel surface subjected to various CCT cycles in the simulated polluted marine environment was investigated using the EIS technique. Figure S1 represents the impedance spectra versus frequency (Nyquist plot). The radius of the capacitive arc of the Nyquist plot is generally taken as a measure of charge transfer resistance
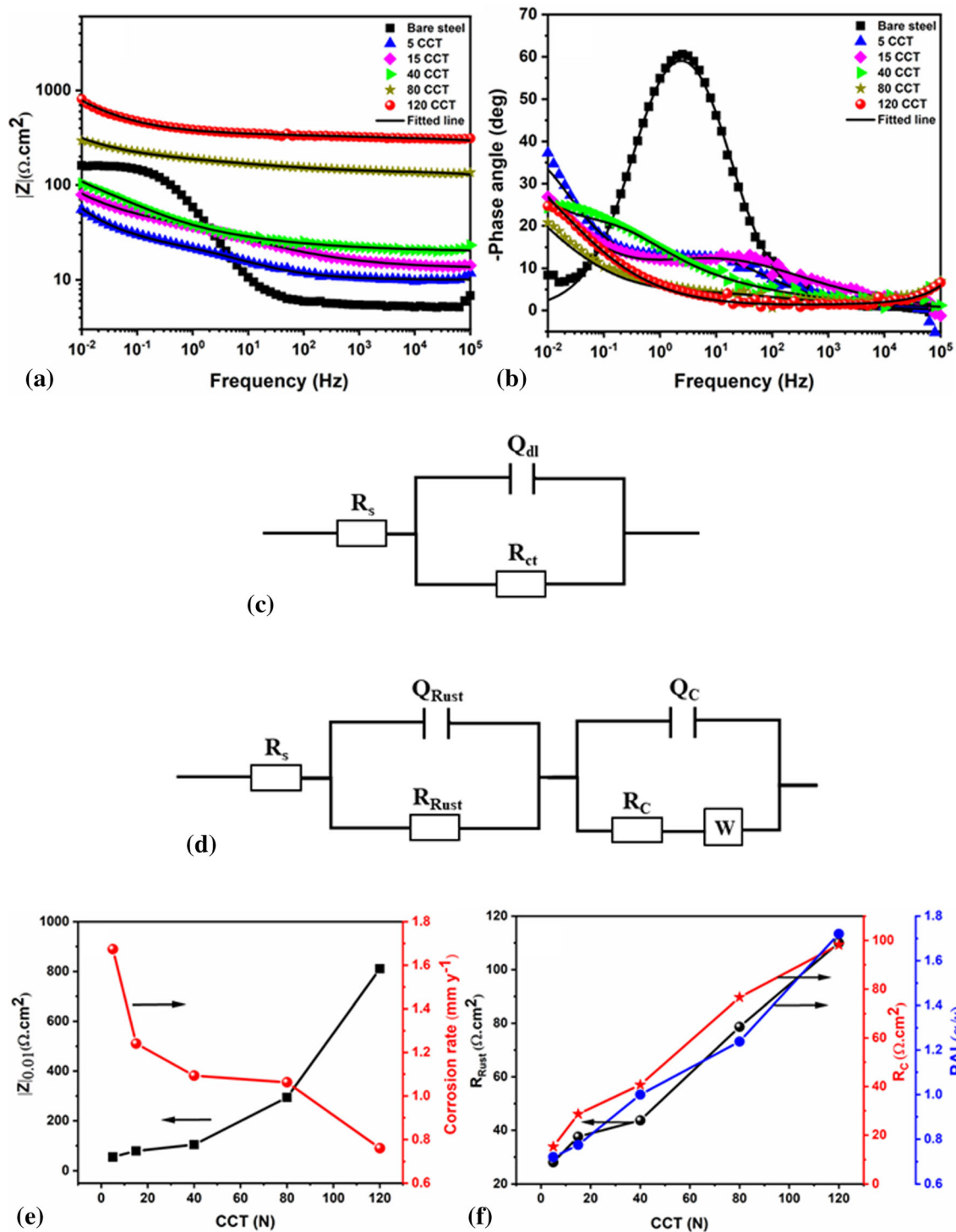
Fig. 9 EIS results of ASTM A572 grade 50 steel in simulated polluted marine environment (a) modulus $|Z|$ vs. frequency (b) phase angle vs. frequency. EEC used for EIS data fittings at different CCT (c) bare steel and (d) rusted steel at 5, 15, 40, 80, and 120 cycles. R_s, R_{rust}, and R_C represent the solution resistance, polarization resistance of the rust layer and resistance to cathodic reactions (e.g., HER/ORR), respectively. Q_C, Q_{rust} and Q_{dl} refers to the constant phase elements (CPE) at the respective electrode and electrolyte interface. W refers to the Warburg impedance due to diffusion. Variations of $|Z|_{0.01}$ and corrosion rate (e), and R_{Rust}, R_C and PAI (f) with CCT number

(R_C) for the auxiliary reaction occurring on the oxide surface at the OCP. Clearly, from Fig. S1, it is observed that the capacitive arc radius increases with the CCT number. This implies that the R_C increases with the CCT number, indicating the oxide surface is more noble or insulating. Figure 9(a) and (b) shows the Bode plots for the bare and rusted steel samples in the simulated polluted marine environment. The electrochemical parameters of rust layer evolution in simulated polluted marine environment were determined by fitting the EIS data with appropriate electrical equivalent circuits (EEC). Based on the following

discussion, a separate EEC was suggested for fitting EIS results of the bare and rusted steel, as presented in Fig. 9(c) and (d). The components present in EEC for the bare steel were polarization resistance (R_p) due to the dissolution of steel substrate and CPE (Q_{dl}). However, the EEC used for steel samples with oxide layers is depicted in Fig. 9(d). As the rust layer uniformly covers the entire surface of the steel, it limits the diffusion of oxygen (presented by the Warburg, W). Besides, the reduction of the rust layer (γ-FeOOH to α-FeOOH phase), represented by R_{Rust}, also contributes to the cathodic reaction in rusted steel along with the other cathodic processes such as HER (R_C). The EEC for these samples, therefore, was modeled using ($Q_{Rust}R_{Rust}$) and ($Q_C R_C W$) as primary components. The parameters obtained after the fitting of the impedance data are given in Tables 4 and 5, with a fitting quality ($\chi^2 < 10^{-4}$).

From Fig. 9(a) and (b), most notably, the high-frequency impedance ($|Z|_{HF}$) increased by more than an order of magnitude with the increase in the number of CCT cycles (Fig. 9a). In the case of the bare uncorroded steel sample, $|Z|_{HF}$ has contribution only from the solution resistance of the electrolyte (R_s). However, the samples subjected to varying numbers of CCT cycles were covered with the rust layers; then, the measured $|Z|_{HF}$ had a contribution from both the electrical resistance of the rust layer and the R_s. Combinedly, $|Z|_{HF}$ in case of samples with rust layer can be termed as equivalent series resistance (R_{ESR}) (Ref 56-58). The observed increase in $|Z|_{HF}$ with the CCT cycle can, therefore, be attributed to the possible increase in the electrical resistance of the rust layer formed since any change in the R_s was expected to be nominal. From Fig. 9(a), for the 80 and 120 CCT, a significant increase in the high-frequency R_{ESR} value was observed. The increase in the electrical resistance can be correlated to the increase in the thickness of the rust layers (Fig. 7) and the nature of the phases formed (Figure 5 and 6), as discussed under the OCP result and sections preceding. In summary, the phase fraction of the more conductive phase, γ-FeOOH, decreased, and that of less conducting α-FeOOH increased with the CCT cycle, and hence the increase in $|Z|_{HF}$.

The value of low-frequency modulus, $|Z|_{LF}$ is a measure of the polarization resistance the corrosion process must overcome across the metal-solution interface (Ref 30, 59). From Fig. 9(a) the value of $|Z|_{LF}$ for the bare steel sample is found to be 161.05 Ω cm^2, which was higher than 55.12 Ω cm^2 at 5 CCT and 78.9 Ω cm^2 at 15 CCT. The plot of the low-frequency impedance, $|Z|_{0.01}$, at 0.01 Hz with CCT cycles in Fig. 9(e) represents the trend more apparently. Correspondingly, the corrosion rate decreased with CCT cycles, which corroborates well with the trend of $|Z|_{0.01}$.

The low-frequency impedance ($|Z|_{LF}$) for rusted samples was the sum of polarization resistance of the rust layer (R_{Rust}) and charge transfer resistance to the cathodic side reactions taking place on the surface of the rust, e.g., HER (designated as, R_C) (Ref 60). While the formation of a very thin rust layer on the surface of the steel up to 15 CCT must have suppressed the charge transfer due to the metal corrosion process, the formation of the conductive γ-FeOOH in the rust (Fig. 5 and 6) must have promoted the cathodic reduction reactions like ORR and HER on the rust surface. However, as the CCT cycles increased, a more stable, low conducting α-FeOOH phase made up most of the rust layer (Fig. 5 and 6), increasing R_C of the cathodic side reactions on the oxide, and hence increasing the $|Z|_{LF}$ value about fourteen times, e.g., to 810.7 Ω cm^2 at 120 CCT. Besides, the conversion of γ-FeOOH to α-FeOOH phase is an electrochemical reduction process (Ref 14, 25, 30), which also will contribute to the increase $|Z|_{LF}$ as a more stable phase forms at higher CCT. The value of R_{Rust} increases at a rapid rate at higher CCT. The increasing trend in R_{Rust} and R_C with CCT cycles shown in Fig. 9(f) is consistent with the above explanation. Besides, from the phase angle plot (Fig. 9b), the bare steel shows a peak at 2.51 Hz with a phase angle of 60.58°. As the CCT cycle increased, the phase angle shifted to a lower frequency for the steel surfaces with rust layers, indicating that the surface behaved more resistively (Ref 61-63), which supports the increase in the $|Z|_{LF}$. Thus, the change in the rust layer composition with CCT cycles stabilized the layer and inhibited both the cathodic reduction reactions and anodic metal dissolution processes, polarizing the charge transfer process on the rust layer and hence increasing overall $|Z|_{LF}$ value.

3.4 Mott–Schottky Analysis

The nature of the defect in the rust layer and its relation to corrosion protection was determined by Mott–Schottky (MS) analysis (Ref 64-66). The iron oxides and oxyhydroxides on the steel surface generally behave as n-type semiconductors (Ref 67, 68), except Fe_3O_4. The MS relationship for n and p-type semiconductors is given as follows (Ref 69-71):

Table 4 Fitting results of the EIS data of bare steel specimen

| CCT cycle | R_S, Ω cm^2 | Q_{dl}, mS s^n cm^{-2} | | R_{ct}, Ω cm^2 |
		Y_{dl}	n_{dl}	
Blank	5.477	3.232×10^{-3}	0.87	158.5

Table 5 Fitting results of EIS data of rusted steel specimens at various CCT numbers

| CCT cycle | R_S, Ω cm^2 | Q_{Rust}, mS s^n cm^{-2} | | R_{Rust}, Ω cm^2 | Q_C, mS s^n cm^{-2} | | R_C, Ω cm^2 | Y_W, mS s$^{0.5}$ cm^{-2} |
		Y_{Rust}	n_{Rust}		Y_C	n_C		
5 CCT	10.04	1584×10^{-3}	0.9	28.1	11.89×10^{-3}	0.54	15.2	120.4×10^{-3}
15 CCT	13.28	9.657×10^{-3}	0.39	37.6	119.2×10^{-3}	0.76	28.7	53.23×10^{-3}
40 CCT	19.81	31.46×10^{-3}	0.28	43.7	36.78×10^{-3}	0.69	40.7	61.38×10^{-3}
80 CCT	55.73	6.61×10^{-5}	0.8	78.7	3.718×10^{-3}	0.36	76.62	19.77×10^{-3}
120 CCT	143.5	0.537×10^{-3}	0.2	110	3.685×10^{-6}	0.9	98.2	8.081×10^{-3}

$$\frac{1}{C_{SC}^2} = \frac{2}{q\varepsilon\varepsilon_0 N_D A^2}\left(E - E_{fb} - \frac{kT}{q}\right) \qquad \text{(Eq 2)}$$
for $n-$type semiconductor

$$\frac{1}{C_{SC}^2} = -\frac{2}{q\varepsilon\varepsilon_0 N_A A^2}\left(E - E_{fb} - \frac{kT}{q}\right) \qquad \text{(Eq 3)}$$
for $p-$type semiconductor

where N_D and N_A are the donor and acceptor density (cm^{-3}), E_{fb} is the flat band potential, k is the Boltzmann constant, T is the temperature in Kelvin, A is the exposed surface area (cm^2), ε is the dielectric constant of iron oxide and oxyhydroxides ($\varepsilon = 12$) (Ref 72-75), ε_0 is the permittivity of free space (8.854×10^{-14} F cm^{-1}), q is the charge of the electron. The charge carrier densities were determined from the slope of the plot (C_{SC}^{-2} vs E). The thickness of the space charge layer (δ_{SC}) for n-type semiconductors was determined from the following relation (Ref 65, 68).

$$\delta_{SC} = \sqrt{\frac{2\varepsilon\varepsilon_0}{qN_D}\left(E - E_{fb} - \frac{kT}{q}\right)} \qquad \text{(Eq 4)}$$

The thickness of the space charge layer (δ_{SC}) is proportional to the ($\frac{1}{C_{SC}^2}$) as per the relation (Ref 68):

$$\delta_{SC} = \varepsilon\varepsilon_0\sqrt{\frac{1}{C_{SC}^2}} \qquad \text{(Eq 5)}$$

Figure 10 shows the MS plots obtained on the steel specimens exposed to different CCT levels in the simulated polluted marine environment.

According to Fig. 10, the rusts on the steel specimens exposed to all CCT cycles showed a dominant n-type behavior. For exposure to 5, 15, and 80 CCT, an n-type behavior and 40 and 120 CCT showed a dominant n- and with a limited p-type behavior. The n-type behavior during all CCT can be attributed to the formation of iron oxides and oxyhydroxides such as α-FeOOH and Fe$_2$O$_3$, which are generally dominant donor species of oxygen vacancies (Ref 67, 68). The minimal p-type behavior can be attributed to oxide phases with cation vacancies (Ref 40, 68). The slope of the n-type component in the MS plots varies with CCT cycles, from which donor density (N_D) was calculated. The higher slope indicated a lower concentration of defects as per Eq (2). The relationship between donor density and thickness of the space charge layer (δ_{SC}) with the CCT cycle was used to derive clarity on the nature and the composition of the rust layer, as shown in Fig. 11.

Clearly, the defect density (N_D) of the rust layer reduced with the wet/dry cyclic corrosion process (Fig. 11), indicating the formation of a compact, dense rust layer comprising of electrochemically stable phase of α-FeOOH (Fig. 5b). This corroborates the findings of EIS in Fig. 9, where the low impedance ($|Z|_{0.01}$) increased with the CCT number. As the defect concentration decreased, the space charge thickness increased (capacitance decreased) indicating a more resistive character, i.e., increase in the charge transfer resistance (R_{Rust} and R_C). This results in a decrease in the interfacial reactions which leads to an increase in corrosion protection ability. At 40 CCT, the slope at more positive potential is used to measure the value of N_D; this is due to the formation of a stable and compact rust layer at noble potential in the form of Fe$_2$O$_3$ and
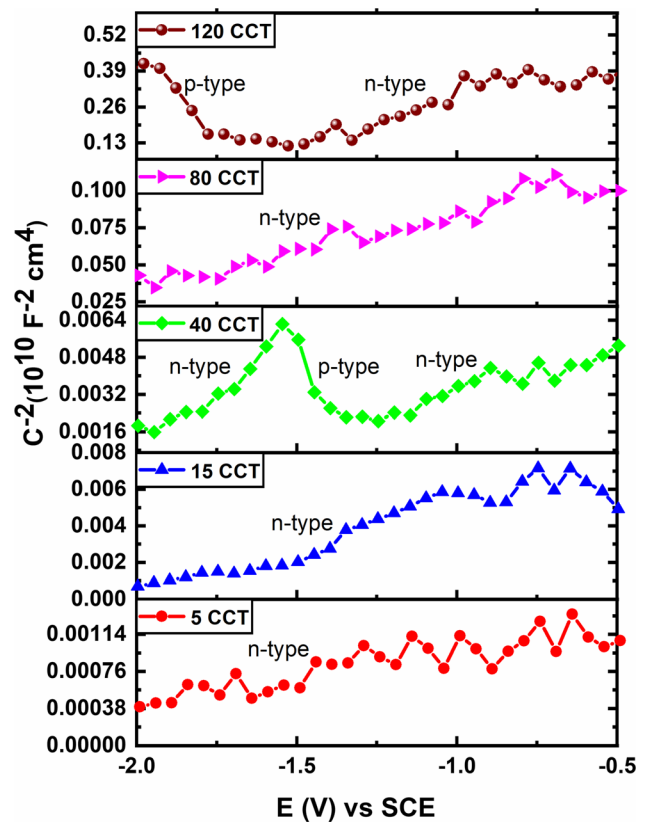

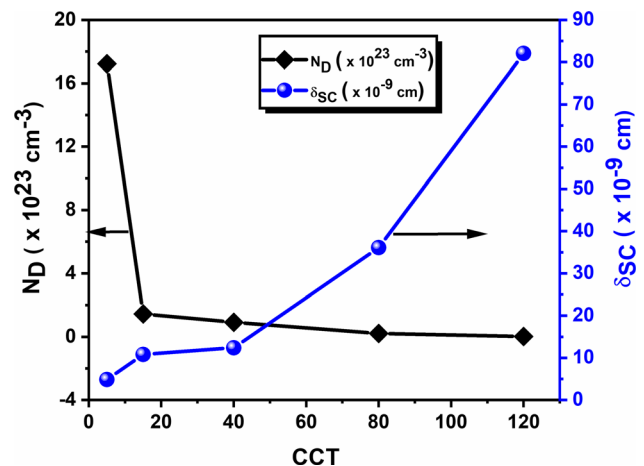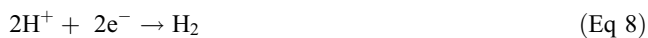**Fig. 10** Shows the MS plots of steel samples exposed to different CCT numbers in a simulated polluted marine environment
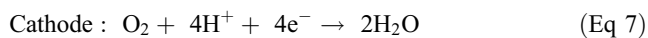

Fig. 11 Shows the relationship between N_D and δ_{SC} with the CCT number during wet/dry cyclic corrosion

α-FeOOH which generally shows n-type character. As the rust layer continuously gets deposited with the progress of the wet/dry cycle, the thickness of the space charge layer (δ_{SC}) increases.

3.4.1 Corrosion Mechanisms. On the basis of corrosion kinetics studied, rust layer characterization, and EIS measurements, the corrosion mechanism of steel samples in the simulated polluted marine environment may be elucidated. The power law model (Fig. 4 and Table 2) could accurately explain the atmospheric corrosion behavior of steel. The

corrosion rate initially increased and then decreased as the CCT progressed, owing to the formation of an adherent rust layer on the surface of the steel sample. Stability in the corrosion rate was observed beyond 17 CCT, with slight fluctuations attributed to the process of continuous breaking and formation of the rust layer (Ref 14, 15). The corrosion rate decreases rapidly after 80 CCT, mainly due to the formation of a thicker and dense rust layer.
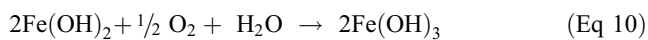
Possible reactions occurring on steel surfaces during initial exposure are shown in Eq (6-8). As the thin layer of the simulated medium was highly aerated and acidic in nature the reactions Eq (7) and (8) are not expected to limit the corrosion kinetics of the steel, whereas the charge transfer step for iron oxidation is expected to be a rate-controlling step, (Eq 6) (Ref 61, 62).
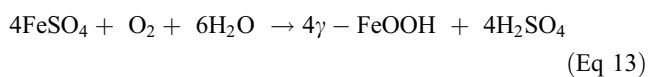
$$\text{Anode}: \text{Fe} \rightarrow \text{Fe}^{2+} + 2e^- \qquad (\text{Eq } 6)$$

$$\text{Cathode}: O_2 + 4H^+ + 4e^- \rightarrow 2H_2O \qquad (\text{Eq } 7)$$

$$2H^+ + 2e^- \rightarrow H_2 \qquad (\text{Eq } 8)$$

Subsequently, the active Fe^{2+} ion generated during anodic dissolution reacted with the OH^- ions formed due to the reaction in Eq (7) and enriched due to the depletion of H^+ ions due to the reaction in Eq (8) to form $Fe(OH)_2$, as illustrated in Eq (9)

$$Fe^{2+} + 2OH^- \rightarrow Fe(OH)_2 \qquad (\text{Eq } 9)$$

As the $Fe(OH)_2$ is unstable, it further oxidizes to form various iron oxyhydroxides such as $Fe(OH)_3$, γ-FeOOH (Eq 10-11) (Ref 60).

$$2Fe(OH)_2 + {}^1\!/_2 O_2 + H_2O \rightarrow 2Fe(OH)_3 \qquad (\text{Eq } 10)$$

$$4Fe(OH)_2 + O_2 \rightarrow 4\gamma - FeOOH + 2H_2O \qquad (\text{Eq } 11)$$

Chen et al. (Ref 20) have proposed that the acidified sulfate can modify the rust formation in the following manner:

$$Fe^{2+} + SO_4^{2-} \rightarrow FeSO_4 \qquad (\text{Eq } 12)$$

$$4FeSO_4 + O_2 + 6H_2O \rightarrow 4\gamma - FeOOH + 4H_2SO_4 \qquad (\text{Eq } 13)$$

$$2H_2SO_4 + O_2 + 2Fe \rightarrow FeSO_4 + 2H_2O \qquad (\text{Eq } 14)$$

It is suggested that the lepidocrocite phase, i.e., γ-FeOOH formed in the rust layer during the initial stages of corrosion, is electrochemically unstable as opposed to a stable α-FeOOH (Ref 76). Therefore, the former transforms into Fe_3O_4 during prolonged wetting-drying cycles as shown below (Ref 14, 77).

$$8\gamma - FeOOH + Fe^{2+} + 2e^- \rightarrow 3Fe_3O_4 + 4H_2O \quad (\text{Eq } 15)$$
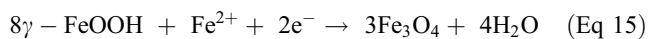
The rust layer formed on the steel surface acts as a barrier for oxygen transport causing a reduction in the corrosion rate of the steel. The cathodic reaction process can continue on the rust surface depending on its composition, e.g., with the formation of conductive oxide phases. The reduction process on the rust, thus, involves the reduction of the rust layer and hydrogen evolution reaction—the most feasible cathodic reaction being H^+ reduction (HER) in this case. The Fe_3O_4 can also get oxidized to α-FeOOH by the ferric ions present in the solution (Eq (16)) as revealed by the micro-Raman spectroscopy (Fig. 6) (Ref 65, 78-80),

$$2Fe_3O_4 + 2Fe(OH)_3 + {}^1\!/_2 O_2 \rightarrow 6\alpha - FeOOH + Fe_2O_3 \qquad (\text{Eq } 16)$$
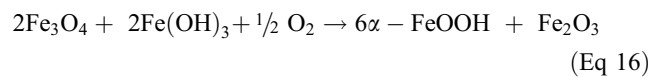
On long-term exposure, γ-FeOOH can also transform into α-FeOOH via the formation of $FeO_x(OH)_{3-2x}$, an intermediate amorphous phase (Ref 10).

$$\gamma - FeOOH \rightarrow FeO_x(OH)_{3-2x} \rightarrow \alpha - FeOOH \qquad (\text{Eq } 17)$$
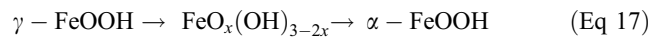
Formation of such an electrochemically stable phase, α-FeOOH, as illustrated in Eq (16) and (17) in the rust layer inhibits the rust layer reduction process that is possible through the reaction shown in equation Eq (15). This in turn reduces the corrosion rate of the steel. This was revealed by higher $|Z|_{0.01}$ and R_{Rust} values shown by the steel exposed to a longer period of exposure (Fig. 9e and f).

Based on the above results and discussion, the evolution of the rust layer with increasing CCT number for an ASTM A572 grade 50 high-strength low-alloy structural steel in a simulated polluted marine environment is schematically shown in Fig. 12.

The rust layer formed on the steel after 5 CCT (Stage-I) (Fig. 12a) consists primarily of γ-FeOOH and Fe_3O_4, with a minor amount of α-FeOOH, corroborating the findings of the GI-XRD results (Fig. 5). The formation of the rust layer reduces the number of oxygen reduction sites on the metal but promotes the reduction of highly unstable and conductive phases such as γ-FeOOH and Fe_3O_4 in the rust layer, which aids the increase in the corrosion rate (Fig. 3). At 15 CCT, (Stage-II) (Fig. 12b), the rust layer thickened and was mostly composed of γ-FeOOH and Fe_3O_4. After 40 CCT, (Stage-III), the rust layer had a dual structure, with the inner layer mostly consisting of α-FeOOH and the outer layer mostly consisting of γ-FeOOH (Fig. 12c). As a stable phase, the inner α-FeOOH mostly protects the steel substrate from corrosion, which stabilized and formed a dense, compact, and adherent inner rust layer on the metal substrate after 120 CCT (Stage-IV) (Fig. 12d). This prevented the diffusion of oxygen and aggressive anions such as Cl^- and SO_4^{2-} onto the metal surface. The outer layer, composed of γ-FeOOH, transforms to α-FeOOH after prolonged exposure (Fig. 5b). Thus, the gradual formation and transformation of the rust layer inhibits the cathodic and anodic reactions, lowering the overall corrosion rate and protecting the steel substrate. This was supported by the EIS results (Table 5), which showed that the R_C and R_{Rust} values increased as the CCT number increased. The MS results also showed a decrease in the defect density and an increase in the thickness of the space charge layer with CCT number. Cracks are generally formed on the rust phases, which are unstable/metastable in nature and are susceptible to reduction during the wetting stage. The cracks in the rust layer will always move from the inner to the outer layer as CCT progresses, owing to the formation of a stable phase (α-FeOOH) in the inner layer.

4. Conclusions

This paper presents the evolution of the nature and structure of the rust layer formed on the A572 grade 50 high-strength low-alloy structural steel in a simulated polluted marine
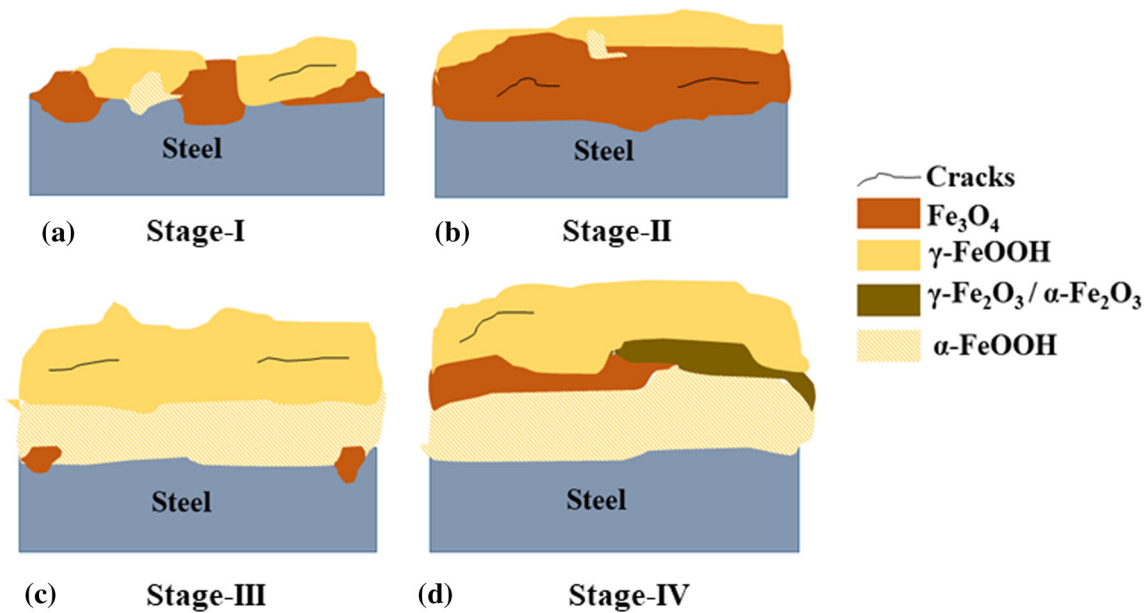
Fig. 12 Schematic of the rust layer evolution in ASTM A572 grade 50 high-strength low-alloy structural steel at (a) Stage-I (5 CCT), (b) Stage-II (15 CCT), (c) Stage-III (40 CCT), and (d) Stage-IV (120 CCT) in a simulated polluted marine environment

atmosphere. The conclusions drawn from the study can be summarized as follows:

(i) Four distinct stages in the corrosion of the steel were observed during the cyclic exposure test to a simulated polluted marine atmosphere.

(ii) The nature of the rust layer formed at each stage was investigated and related to the corrosion behavior in different stages. Results showed that at higher CCT, the rust layer becomes more stable and compact due to the predominance of the α-FeOOH phase and the decrease in the fraction of γ-FeOOH. The former results in the increase in the protectiveness of the rust layer (hence the decrease in the corrosion rate) with the increase in the CCT cycles.

(iii) From the Raman point scan along the thickness of the oxide layer grown at lower CCT cycle, γ-FeOOH phase was found to be dominated at all depth. At higher exposure cycle, i.e., 120 CCT, the α-FeOOH phase was found at all depths of the rust layer of the sample. Since the γ-FeOOH phase is metastable and less protective, a very low PAI value was observed at smaller CCT cycles.

(iv) The deeper penetration of the chloride ion in the rust layer, even reaching the substrate, was found when the latter was dominated by γ-FeOOH phase than α-FeOOH phase. In case of α-FeOOH dominated rust layer, the chloride ion is limited to only the outer surface, even after longer exposure.

(v) The developed rust layer in the samples exposed to higher CCT cycles was nobler, with a relatively high positive OCP. The decrease in the phase fraction of the more conductive phase, γ-FeOOH, and the increase in that of less conducting α-FeOOH with the CCT cycle, was responsible for the suppression of the cathodic processes aiding the corrosion of the steel, which resulted in lowering the corrosion rate as the exposure cycles were increased. This explained the higher protectiveness

of the rust layers formed at higher CCT cycles. This observation was corroborated from the EIS and Mott–Schottky analysis.

(vi) Finally, the corrosion and the process of rust layer development on the steel samples in the simulated polluted marine environment were elucidated with a plausible mechanism based on the corrosion kinetics studies, rust layer characterizations, and EIS measurements.

Data availability

The data supporting this study's findings are available from the corresponding author, upon reasonable request.

Conflict of interest

The authors affirm that they have no known financial or interpersonal conflicts that would have appeared to have an impact on the research presented in this study.

References

1. L. Silvestre, P. Langenberg, T. Amaral, M. Carboni, M. Meira, and A. Jordão (2016) Use of niobium high strength steels with 450 MPA yield strength for construction, in *HSLA Steels 2015, Microalloying 2015 &*

Offshore Engineering Steels 2015, 1, Nov 11th–13th, 2015 (China). Springer, p 931–939

2. L. Silvestre, R. Pimenta, M. Nogueira, L. Queiroz, H. Salles, A. Jordão, R. Ribeiro, M. Pimenta, J. Conceição, L. Rocha, and F. Buratto, High Strength Steel as a Solution for the Lean Design of Industrial Buildings, *J. Mater. Res. Technol.*, 2012, **1**(1), p 35–41

3. E. Olorundaisi, T. Jamiru, and A.T. Adegbola, Mitigating the Effect of Corrosion and Wear in the Application of High Strength Low Alloy Steels (HSLA) in the Petrochemical Transportation Industry: A review, *Mater. Res. Express*, 2020, **6**(12), p 1265k9

4. S. Keeler and M. Kimchi, *Advanced High-Strength Steels Application Guidelines V5.0*, WorldAutoSteel, 2015

5. M. Natesan, S. Muralidharan, and N. Palaniswamy, Atmospheric Corrosion Performance of Engineering Materials in India, *NACE International*, 2010, **49**(8), p 60–66

6. Y. Xu, Y. Huang, F. Cai, D. Lu, and X. Wang, Study on Corrosion Behavior and Mechanism of AISI 4135 Steel in Marine Environments Based on Field Exposure Experiment, *Sci. Total. Environ.*, 2022, **830**, 154864

7. Z.L. Li, K. Xiao, C.F. Dong, X.Q. Cheng, W. Xue, and W. Yu, Atmospheric Corrosion Behavior of Low-Alloy Steels in a Tropical Marine Environment, *J. Iron. Steel Res. Int.*, 2019, **26**(12), p 1315–1328

8. P. Murkute, R. Kumar, S. Choudhary, H.S. Maharana, J. Ramkumar, and K. Mondal, Comparative Atmospheric Corrosion Behavior of a Mild Steel and an Interstitial Free Steel, *J. Mater. Eng. Perform.*, 2018, **27**(9), p 4497–4506

9. Y. Fan, W. Liu, S. Li, T. Chowwanonthapunya, B. Wongpat, Y. Zhao, B. Dong, T. Zhang, and X. Li, Evolution of Rust Layers on Carbon Steel and Weathering Steel in High Humidity and Heat Marine Atmospheric Corrosion, *J. Mater. Sci. Technol.*, 2020, **39**, p 190–199

10. M. Yamashita, H. Miyuki, Y. Matsuda, H. Nagano, and T. Misawa, The Long Term Growth of the Protective Rust Layer Formed on Weathering Steel by Atmospheric Corrosion during a Quarter of a Century, *Corros. Sci.*, 1994, **36**(2), p 283–299

11. S.J. Oh, D.C. Cook, and H.E. Townsend, Atmospheric Corrosion of Different Steels in Marine, Rural and Industrial Environments, *Corros. Sci.*, 1999, **41**(9), p 1687–1702

12. D.D. Singh, S. Yadav, and J.K. Saha, Role of Climatic Conditions on Corrosion Characteristics of Structural Steels, *Corros. Sci.*, 2008, **50**(1), p 93–110

13. F. Wu, Z. Hu, X. Liu, C. Su, and L. Hao, Understanding in Compositional Phases of Carbon Steel Rust Layer with a Long-Term Atmospheric Exposure, *Mater. Lett.*, 2022, **315**, 131968

14. W. Zhu, Y. Zhao, Y. Feng, J. Cui, Z. Chen, and L. Chen, Structure and Electrochemical Behavior of the Rust on 690 MPa Grade Construction Steel in a Simulated Industrial Atmosphere, *Metall. Mater. Trans. A*, 2022, **53**(8), p 3044–3056

15. B. Liu, X. Mu, Y. Yang, L. Hao, X. Ding, J. Dong, Z. Zhang, H. Hou, and W. Ke, Effect of Tin Addition on Corrosion Behavior of a Low-Alloy Steel in Simulated Costal-Industrial Atmosphere, *J. Mater. Sci. Technol.*, 2019, **35**(7), p 1228–1239

16. U.R. Evans and C.A. Taylor, Mechanism of Atmospheric Rusting, *Corros. Sci.*, 1972, **12**(3), p 227–246

17. X. Feng, X. Lu, Y. Zuo, N. Zhuang, and D. Chen, The Effect of Deformation on Metastable Pitting of 304 Stainless Steel in Chloride Contaminated Concrete Pore Solution, *Corros. Sci.*, 2016, **103**, p 223–229

18. Y. Lu, J. Dong, and W. Ke, Effects of Cl^- Ions on the Corrosion Behaviour of Low Alloy Steel in Deaerated Bicarbonate Solutions, *J. Mater. Sci. Technol.*, 2016, **32**(4), p 341–348

19. Y.F. Cheng, M. Wilmott, and J.L. Luo, The Role of Chloride Ions in Pitting of Carbon Steel Studied by the Statistical Analysis of Electrochemical Noise, *Appl. Surf. Sci.*, 1999, **152**(3–4), p 161–168

20. W. Chen, L. Hao, J. Dong, and W. Ke, Effect of Sulphur Dioxide on the Corrosion of a Low Alloy Steel in Simulated Coastal Industrial Atmosphere, *Corros. Sci.*, 2014, **83**, p 155–163

21. H. Cano, D. Neff, M. Morcillo, P. Dillmann, I. Diaz, and D. de la Fuente, Characterization of Corrosion Products Formed on Ni 2.4 wt.%-Cu 0.5 wt.%-Cr 0.5 wt.% Weathering Steel Exposed in Marine Atmospheres, *Corros. Sci.*, 2014, **87**, p 438–451

22. C. Rémazeilles, M. Saheb, D. Neff, E. Guilminot, K. Tran, J.A. Bourdoiseau, R. Sabot, M. Jeannin, H. Matthiesen, P. Dillmann, and P. Refait, Microbiologically Influenced Corrosion of Archaeological Artefacts: Characterization of Iron (II) Sulfides by Raman Spectroscopy, *J. Raman Spectrosc.*, 2010, **41**(11), p 1425–1433

23. S.J. Oh, D.C. Cook, and H.E. Townsend, Characterization of Iron Oxides Commonly Formed as Corrosion Products on Steel, *Hyperfine Interact.*, 1998, **112**(1), p 59–66

24. A. Artigas, A. Monsalve, K. Sipos, O. Bustos, J. Mena, R. Seco, and N. Garza-Montes-de-Oca, Development of Accelerated Wet–Dry Cycle Corrosion Test in Marine Environment for Weathering Steels, *Corros. Eng. Sci. Technol.*, 2015, **50**(8), p 628–632

25. T. Nishimura, H. Katayama, K. Noda, and T. Kodama, Electrochemical Behavior of Rust Formed on Carbon Steel in a Wet/Dry Environment Containing Chloride Ions, *Corrosion (Houston, TX, U. S.)*, 2000, **56**(9), p 935–941

26. X. Liu, Y. Sui, J. Zhou, Y. Liu, X. Li, and J. Hou, Influence of Available Chlorine on Corrosion Behaviour of Low Alloy Marine Steel in Natural Seawater, *Corros. Eng. Sci. Technol.*, 2023, **58**, p 1–7

27. B. Zhang, W. Liu, Y. Sun, W. Yang, L. Chen, J. Xie, and W. Li, Corrosion Behavior of the 3 wt.% Ni Weathering Steel with Replacing 1 wt.% Cr in the Simulated Tropical Marine Atmospheric Environment, *J. Phys. Chem. Solids*, 2023, **175**, p 111221

28. T. Zhang, L. Hao, Z. Jiang, C. Liu, L. Zhu, X. Cheng, Z. Liu, N. Wang, and X. Li, Investigation of Rare Earth (RE) on Improving the Corrosion Resistance of Zr-Ti Deoxidized Low Alloy Steel in the Simulated Tropic Marine Atmospheric Environment, *Corros. Sci.*, 2023, **19**, 111335

29. R.F. Assumpção, V.C. Campideli, V.F. Lins, and D.C. Sicupira, Comparative Analysis on Corrosion Behavior of Si-Based Weathering Steels in a Simulated Industrial Atmosphere, *J. Mater. Eng. Perform.*, 2023, **11**, p 1–9

30. Y. Fan, W. Liu, Z. Sun, T. Chowwanonthapunya, Y. Zhao, B. Dong, T. Zhang, and W. Banthukul, Effect of Chloride Ion on Corrosion Resistance of Ni-Advanced Weathering Steel in Simulated Tropical Marine Atmosphere, *Constr. Build. Mater.*, 2021, **266**, 120937

31. B. Dong, W. Liu, T. Zhang, L. Chen, Y. Fan, Y. Zhao, H. Li, W. Yang, and Y. Sun, Clarifying the Effect of a Small Amount of Cr Content on the Corrosion of Ni-Mo Steel in Tropical Marine Atmospheric Environment, *Corros. Sci.*, 2023, **210**, 110813

32. L. Hao, S. Zhang, J. Dong, and W. Ke, Atmospheric Corrosion Resistance of MnCuP Weathering Steel in Simulated Environments, *Corros. Sci.*, 2011, **53**(12), p 4187–4192

33. A.L. Rudd and C.B. Breslin, The Influence of Ultraviolet Illumination on the Passive Behavior of Zinc, *J. Electrochem. Soc.*, 2000, **147**(4), p 1401

34. N.E. Hakiki, M.D. Belo, A.M. Simoes, and M.G. Ferreira, Semiconducting Properties of Passive Films Formed on Stainless Steels: Influence of the Alloying Elements, *J. Electrochem. Soc.*, 1998, **145**(11), p 3821

35. E. Sikora and D.D. Macdonald, The Passivity of Iron in the Presence of Ethylenediaminetetraacetic Acid I. General Electrochemical Behavior, *J. Electrochem. Soc.*, 2000, **147**(11), p 4087

36. S. Ningshen, U.K. Mudali, V.K. Mittal, and H.S. Khatak, Semiconducting and Passive Film Properties of Nitrogen-Containing Type 316LN Stainless Steels, *Corros. Sci.*, 2007, **49**(2), p 481–496

37. M.F. Montemor, M.G. Ferreira, N.E. Hakiki, and M.D. Belo, Chemical Composition and Electronic Structure of the Oxide Films Formed on 316L Stainless Steel and Nickel Based Alloys in High Temperature Aqueous Environments, *Corros. Sci.*, 2000, **42**(9), p 1635–1650

38. C. Sunseri, S. Piazza, and F. Di Quarto, Photocurrent Spectroscopic Investigations of Passive Films on Chromium, *J. Electrochem. Soc.*, 1990, **137**(8), p 2411

39. A.M. Simoes, M.G. Ferreira, B. Rondot, and M. da Cunha Belo, Study of Passive Films Formed on AISI 304 Stainless Steel by Impedance Measurements and Photo Electrochemistry, *J. Electrochem. Soc.*, 1990, **137**(1), p 82

40. M. Sun, K. Xiao, C. Dong, X. Li, and P. Zhong, Effect of pH on Semiconducting Property of Passive Film Formed on Ultra-High-Strength Corrosion-Resistant Steel in Sulfuric Acid Solution, *Metall. Mater. Trans. A*, 2013, **44**(10), p 4709–4717

41. J.W. Schultze and M.M. Lohrengel, Stability, Reactivity and Breakdown of Passive Films. Problems of Recent and Future Research, *Electrochim. Acta*, 2000, **45**(15–16), p 2499–2513

42. M. Pourbaix, The linear bilogarithmic law for atmospheric corrosion, in *Atmospheric Corrosion, Hollywood, FL, Oct. 5–10, Proceedings*, 1982, p 107–121

43. S. Feliu and M. Morcillo, Atmospheric corrosion testing in Spain, atmospheric corrosion, corrosion monograph series, *The Electrochemical Society*. W.H. Ailor Ed., Inc, Princeton, 1982

44. M. Benarie and F.L. Lipfert, A General Corrosion Function in Terms of Atmospheric Pollutant Concentrations and Rain pH, *Atmos. Environ. (1967–1989)*, 1986, **20**(10), p 1947–1958

45. M. Morcillo, B. Chico, I. Díaz, H. Cano, and D. De la Fuente, Atmospheric Corrosion Data of Weathering Steels: A Review, *Corros. Sci.*, 2013, **77**, p 6–24

46. M. Morcillo, B. Chico, J. Alcántara, I. Díaz, R. Wolthuis, and D. De la Fuente, SEM/Micro-Raman Characterization of the Morphologies of Marine Atmospheric Corrosion Products Formed on Mild Steel, *J. Electrochem. Soc.*, 2016, **163**(8), p C426

47. D. Kong, C. Dong, X. Ni, L. Zhang, H. Luo, R. Li, L. Wang, C. Man, and X. Li, Superior Resistance to Hydrogen Damage for Selective Laser Melted 316L Stainless Steel in a Proton Exchange Membrane Fuel Cell Environment, *Corros. Sci.*, 2020, **166**, 108425

48. J. Alcántara, B. Chico, J. Simancas, I. Díaz, D. De la Fuente, and M. Morcillo, An Attempt to Classify the Morphologies Presented by Different Rust Phases Formed during the Exposure of Carbon Steel to Marine Atmospheres, *Mater Charact*, 2016, **118**, p 65–78

49. J. Alcántara, B. Chico, I. Díaz, D. De la Fuente, and M. Morcillo, Airborne Chloride Deposit and its Effect on Marine Atmospheric Corrosion of Mild Steel, *Corros. Sci.*, 2015, **97**, p 74–88

50. T. Ohtsuka and S. Tanaka, Monitoring the Development of Rust Layers on Weathering Steel using in Situ Raman Spectroscopy under Wet-and-Dry Cyclic Conditions, *J. Solid State Electrochem.*, 2015, **19**(12), p 3559–3566

51. J. Monnier, L. Bellot-Gurlet, D. Baron, D. Neff, I. Guillot, and P. Dillmann, A methodology for Raman Structural Quantification Imaging and its Application to Iron Indoor Atmospheric Corrosion Products, *J. Raman Spectrosc.*, 2011, **42**(4), p 773–781

52. N. Yucel, A. Kalkanli, and E.N. Caner-Saltik, Investigation of Atmospheric Corrosion Layers on Historic Iron Nails by Micro-Raman Spectroscopy, *J. Raman Spectrosc.*, 2016, **47**(12), p 1486–1493

53. D.L. De Faria, S. Venâncio Silva, and M.T. De Oliveira, Raman Microspectroscopy of Some Iron Oxides and Oxyhydroxides, *J. Raman Spectrosc.*, 1997, **28**(11), p 873–878

54. W. Liu, J. Liu, H. Pan, F. Cao, Z. Wu, H. Lv, and Z. Xu, Synergisic Effect of Mn, Cu, P with Cr Content on the Corrosion Behavior of Weathering Steel as a Train under the Simulated Industrial Atmosphere, *J. Alloys Compd.*, 2020, **834**, 155095

55. K. Kashima, S. Hara, H. Kishikawa, and H. Miyuki, Evaluation of Protective Ability of Rust Layers on Weathering Steels by Potential Measurement, *Zairyo to Kankyo*, 2000, **49**(1), p 15–21. (**in Japanese**)

56. Z. Niu, W. Zhou, J. Chen, G. Feng, H. Li, W. Ma, J. Li, H. Dong, Y. Ren, D. Zhao, and S. Xie, Compact-Designed Supercapacitors using Free-Standing Single-Walled Carbon Nanotube Films, *Energy Environ. Sci.*, 2011, **4**(4), p 1440–1446

57. P.L. Taberna, C. Portet, and P. Simon, Electrode Surface Treatment and Electrochemical Impedance Spectroscopy Study on Carbon/Carbon Supercapacitors, *Appl. Phys. A Mater. Sci. Process.*, 2006, **82**(4), p 639–646

58. N.H. Basri and B.N. Dolah, Physical and Electrochemical Properties of Supercapacitor Electrodes Derived from Carbon Nanotube and Biomass Carbon, *Int. J. Electrochem. Sci.*, 2013, **8**, p 257–273

59. A. Nishikata, Y. Ichihara, and T. Tsuru, An Application of Electrochemical Impedance Spectroscopy to Atmospheric Corrosion Study, *Corros. Sci.*, 1995, **37**(6), p 897–911

60. C. Liu, R.I. Revilla, Z. Liu, D. Zhang, X. Li, and H. Terryn, Effect of Inclusions Modified by Rare Earth Elements (Ce, La) on Localized Marine Corrosion in Q460NH Weathering Steel, *Corros. Sci.*, 2017, **129**, p 82–90

61. Y. Wang, X. Mu, J. Dong, A.J. Umoh, and W. Ke, Insight into Atmospheric Corrosion Evolution of Mild Steel in a Simulated Coastal Atmosphere, *J. Mater. Sci. Technol.*, 2021, **76**, p 41–50

62. Y. Sun, X. Wei, J. Dong, N. Chen, H. Zhao, Q. Ren, and W. Ke, Understanding the Role of Alloyed Ni and Cu on Improving Corrosion Resistance of Low Alloy Steel in the Simulated Beishan Groundwater, *J. Mater. Sci. Technol.*, 2022, **130**, p 124–135

63. M. Hosseini, S.F. Mertens, M. Ghorbani, and M.R. Arshadi, Asymmetrical Schiff Bases as Inhibitors of Mild Steel Corrosion in Sulphuric Acid Media, *Mater. Chem. Phys.*, 2003, **78**(3), p 800–808

64. I.M. Gadala and A. Alfantazi, A Study of X100 Pipeline Steel Passivation in Mildly Alkaline Bicarbonate Solutions Using Electrochemical Impedance Spectroscopy under Potentiodynamic Conditions and Mott–Schottky, *Appl. Surf. Sci.*, 2015, **357**, p 356–368

65. G. Tranchida, F. Di Franco, B. Megna, and M. Santamaria, Semiconducting Properties of Passive Films and Corrosion Layers on Weathering Steel, *Electrochim. Acta*, 2020, **354**, 136697

66. J. Benzakour and A. Derja, Characterisation of the Passive Film on Iron in Phosphate Medium by Voltammetry and XPS Measurements, *J. Electroanal. Chem.*, 1997, **437**(1–2), p 119–124

67. Z. Feng, X. Cheng, C. Dong, L. Xu, and X. Li, Passivity of 316L Stainless Steel in Borate Buffer Solution Studied by Mott–Schottky Analysis, Atomic Absorption Spectrometry and X-Ray Photoelectron Spectroscopy, *Corros. Sci.*, 2010, **52**(11), p 3646–3653

68. Y.S. Kim and J.G. Kim, Corrosion Behavior of Pipeline Carbon Steel under Different Iron Oxide Deposits in the District Heating System, *Metals (Basel Switz.)*, 2017, **7**(5), p 182

69. N.F. Mott, The Theory of Crystal Rectifiers, *Proc. R. Soc. Lond. Ser. A Math. Phys. Sci.*, 1939, **171**(944), p 27–38

70. W. Schottky, On the Semiconductor Theory of Junction and Tip Rectifiers, *Z. Phys. A Part. Fields*, 1939, **113**, p 367–414

71. M.H. Dean and U. Stimming, The Electronic Properties of Disordered Passive Films, *Corros. Sci.*, 1989, **29**(2–3), p 199–211

72. G. Goodlet, S. Faty, S. Cardoso, P.P. Freitas, A.M. Simoes, M.G. Ferreira, and M.D. Belo, The Electronic Properties of Sputtered Chromium and Iron Oxide Films, *Corros. Sci.*, 2004, **46**(6), p 1479–1499

73. S. Ahn and H. Kwon, Diffusivity of Point Defects in the Passive Film on Fe, *J. Electroanal. Chem.*, 2005, **579**(2), p 311–319

74. I.C. Guedes, I.V. Aoki, M.J. Carmezim, M.F. Montemor, M.G. Ferreira, and M.D. Belo, The Influence of Copper and Chromium on the Semiconducting Behaviour of Passive Films Formed on Weathering Steels, *Thin Solid Films*, 2006, **515**(4), p 2167–2172

75. L. Hamadou, A. Kadri, and N. Benbrahim, Impedance Investigation of Thermally Formed Oxide Films on AISI 304L Stainless Steel, *Corros. Sci.*, 2010, **52**(3), p 859–864

76. M. Stratmann, K. Bohnenkamp, and H.J. Engell, An Electrochemical Study of Phase-Transitions in Rust Layers, *Corros. Sci.*, 1983, **23**(9), p 969–985

77. H. Tanaka, R. Mishima, N. Hatanaka, T. Ishikawa, and T. Nakayama, Formation of Magnetite Rust Particles by Reacting Iron Powder with Artificial α-, β-and γ-FeOOH in Aqueous Media, *Corros. Sci.*, 2014, **78**, p 384–387

78. S. Nasrazadani and A. Raman, Formation and Transformation of Magnetite (Fe_3O_4) on Steel Surfaces under Continuous and Cyclic Water Fog Testing, *Corrosion (Houston, TX, U. S.)*, 1993, **49**(4), p 294–300

79. T. Ishikawa, Y. Kondo, A. Yasukawa, and K. Kandori, Formation of Magnetite in the Presence of Ferric Oxyhydroxides, *Corros. Sci.*, 1998, **40**(7), p 1239–1251

80. A.B. Pattnaik and S. Parida, Materials degradation: metallic materials, In *New Horizons in Metallurgy, Materials and Manufacturing*, Springer Nature Singapore, Singapore, 2022, p 107–122